Hindawi
Geofluids
Volume 2022, Article ID 1851899, 14 pages
https://doi.org/10.1155/2022/1851899

Research Article

Floor Failure Characteristics in Deep Island Longwall Panel: Theoretical Analysis and Field Verification

Pengpeng Wang,[1,2] Yixin Zhao,[1,2,3] Qingshan Ren,[1,2] Yaodong Jiang,[1,4] Cun Zhang,[1,2] and Yirui Gao[1,2]

[1]*Beijing Key Laboratory for Precise Mining of Intergrown Energy and Resources, China University of Mining and Technology (Beijing), Beijing 100083, China*
[2]*School of Energy and Mining Engineering, China University of Mining and Technology (Beijing), Beijing 100083, China*
[3]*State Key Laboratory of Coal Resources and Safe Mining, China University of Mining and Technology (Beijing), Beijing 100083, China*
[4]*School of Mechanics and Civil Engineering, China University of Mining and Technology (Beijing), Beijing 100083, China*

Correspondence should be addressed to Yixin Zhao; zhaoyx@cumtb.edu.cn

Received 12 October 2021; Accepted 24 February 2022; Published 17 March 2022

Academic Editor: Yong-Zheng Wu

Floor failure in deep coal mining above confined aquifers with high-water pressure may induce floor water inrush disasters. Considering the effects of mining stress and nonuniformly distributed water pressure, a mechanical calculation model of the island longwall panel in up-dip mining was established, and the stress distribution and floor failure characteristics were analyzed. The failure characteristics of the floor at NO. 2129 panel in Xingdong coal mine were detected by the borehole televiewer and microseismic monitoring system to validate the theoretical model. The results indicated that the floor failure characteristics along the strike and inclination of the island longwall panel in up-dip mining were "asymmetric inverted saddle-shaped" and "spoon-shaped," respectively. The maximum floor failure depths before and after roof hydraulic fracturing (RHF) were 45.7 m and 29.1 m, respectively. The theoretical calculation results of the maximum depths of floor failure were 45.1 m and 29.9 m, respectively. The theoretical failure characteristics were consistent with those measured on site. The stress concentration magnitude and floor failure depth on the side of the isolated coal pillar were greater than those of other areas, and the water-inrush-prone zones were concentrated on the side of the isolated coal pillar near the intersection of the working face and the roadway. The research results could provide a certain reference for floor failure and water inrush mechanisms under complex geological conditions in deep mining.

1. Introduction

With the increase of operational coal mining depth in China, the surrounding rock in deep mining is prone to large-scale destabilization or dynamic response damage [1]. Increased range of floor failure zone induced by the coupling of high-water pressure and ground stress as well as strong mining disturbances in deep coal mining [2–6]. Water inrushes occur when floor failure zones are connected with high water pressure aquifers in the overlying strata under the floor [7]. Therefore, it is essential to investigate the floor failure characteristics induced by mining and confined aquifers to manage floor water inrush.

Three methods of theoretical analysis, numerical calculation and on-site monitoring are generally applied to investigate the floor failure characteristics. In terms of theoretical analysis, according to the abutment pressure distribution around the working face, a mechanical model of coal seam floor failure under the abutment pressure induced by coal seam mining was established, and the stress distribution and the maximum failure depth of the coal seam floor during mining were also calculated [8–11]. Xue et al. [12]

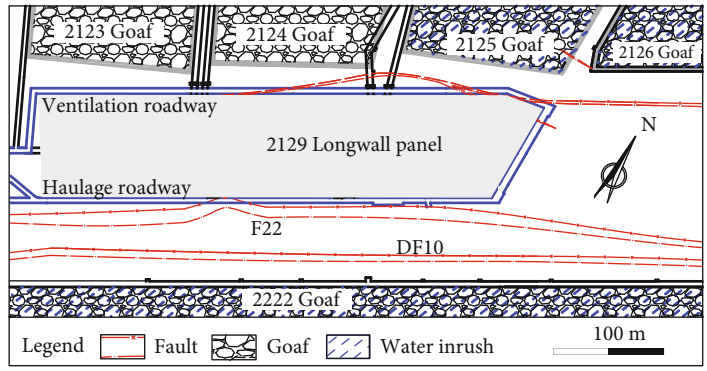

Figure 1: Location of the study area.

established a mechanical calculation model of the floor failure patterns in the strike and dip directions along the working face after mining to study the floor failure characteristics of roof cutting and gob side entry retaining in confined water. The floor rock mass was regarded as a transversely isotropic body and an analytical solution for the floor stress was derived [13–16]. A mechanical model for the floor failure depth in inclined coal seam mining was established to obtain the floor failure characteristics in inclined coal seams as "upper-small-lower-large" [17–19]. Song [19] and Liang et al. [20, 21] established a mechanical model under the combined action of water pressure and mining by considering the actions of high-water pressure and analyzed the stress field and failure characteristics. Ma et al. [5] proposed an improved theoretical model that considered the whole confined aquifer in the floor to analyze the stress distribution and failure zones.

On-site monitoring is a direct and effective method for understanding the extent of damage to the surrounding rock. Currently, the most commonly used field monitoring methods are the borehole water injection, borehole acoustic wave, and borehole imaging as well as borehole strain method [22–25]. In recent years, microseismic monitoring technology has been applied by many scholars to monitor floor damage and water inrush problems. Cheng et al. [26] adopted a microseismic monitoring system to identify the spatial location and formation process of water flow channels. Zhao et al. [27] proposed a set of rock mass seepage channel inversion methods based on microseismic data. Zhou et al. [28] presented a microseismic monitoring analysis method for evaluating potential seepage channels. Ma et al. [5] investigated the evolution characteristics and development pattern of floor failure during high thickness coal seam mining using microseismic monitoring. Cheng et al. [29] examined and calculated the floor disturbance depth through microseismic virtual reality visualization.

Scholars have conducted many investigations and yielded abundant findings in research on the failure characteristics of coal seam floor. Due to the inclination of the coal seam, the failure characteristics of the surrounding rock of the working face are obviously different from those of the horizontal and near horizontal coal seams [2, 30]. In addition, due to the superposition of high stress caused by nearby mined longwall panels, the high-stress concentration zone is formed in the surrounding rock [31]. The large deformation and large-scale failure of floor rock strata are induced by high-stress concentration. Water-conducting channels tend to be formed due to the large-scale and high-intensity stress disturbance induced by repeated mining [24, 32]. The risk of water inrush from coal seam floor in deep island longwall panel increases under deep complex hydrogeological conditions [16]. However, most previous scholars have investigated the floor failure characteristics of longwall mining faces along strikes, and few have addressed the floor failure characteristics of island longwall mining panels in up-dip mining. Therefore, the study of floor failure characteristics of the island longwall panel in up-dip mining above confined water are essential to propose a reasonable method to prevent and control floor water inrush in deep mining.

Therefore, a mechanical model of the island longwall panel in up-dip mining under the combined effect of high-water and mining pressure was established in this paper. The stress distribution in the mining floor rock mass was calculated, and then the floor failure characteristics were obtained based on the Mohr-Coulomb criterion. In addition, the floor failure characteristics before and after RHF were comparatively analyzed, and the results of on-site measurements verified the reasonableness of the theoretical model. The research results could provide a reference for studying the mechanism and prevention of floor water inrush under complex mining geological conditions.

2. Site Descriptions

The Xingdong coal mine is located in the northeastern Hanxing coalfield, Hebei Province, China. Figure 1 shows the general mining layout and the location of the study area. The mining depth of the longwall panel NO. 2129 at Xingdong coal mine is 1027–1125 m and 92.5 m wide, and the lengths of the ventilation and haulage roadways are 416 m and 367 m, respectively. The longwall panel NO. 2129 is an island longwall panel with a goaf on both sides. The ventilation roadway is adjacent to the goafs of longwall panels NOs. 2125–2127, and water inrush occurred in these panels. The ventilation roadway is also adjacent to the longwall panels NO. 2123 and NO. 2124 that do not have floor water inrushes. The average width of coal pillar between ventilation roadway and the goafs is 30 m, which is called narrow

Description	Thickness (m)	Column	Distance (m)
Siltstone, thick layer and dense	14.96		
NO.1 coal	0.35		
Fine sandstone, thick layer and dense	9.55		
Aluminous siltstone	3.6		
Mudstone with plant fossil fragments	0.2		
NO.2 coal	3.95		
Siltstone, medium fine sandstone sandy mudstone and coal seam	47.11		47.11
Yeqing aquifer	2.18		96.59
Mudstone, sandy mudstone, siltstone and coal seam	47.3		140.29
Fuqing aquifer	2.1		161.03
Siltstone, mudstone, medium fine sandstone and coal seam	41.6		176.12
Daqing aquifer	5.06		
Sandstone, mudstone, bauxite mudstone and coal seam	15.68		
Benxi aquifer	3.97		
Bauxite, siltstone and fine sandstone	11.12		
Ordovician limestone aquifer	545		

Figure 2: Stratigraphic column of seam, roof, and floor strata.

coal pillar. The haulage roadway is adjacent to longwall panel NO. 2222 with floor water inrush and the F22 and DF10 normal faults. The fault drops are 9–58 m and 8–40 m, respectively. The average width of the coal pillar between the haulage roadway and the goaf of longwall panel NO. 2222 is 74 m, which is called wide coal pillar. The updip longwall mining is adopted, and the roof is managed by the caving method. The average thickness of coal seam #2 is 3.95 m, dipping at an angle of 9°–14°, with an average of 11°. According to the stratigraphic column diagram of the Xingdong coal mine (Figure 2), the lithology of the overlying strata is fine sandstone, sandy mudstone, and siltstone, and the floor strata are fine sandstone and sandy mudstone. There are five aquifers in the floor of coal seam #2. The aquifers are the Yeqing, Fuqing, Daqing, Benxi, and Ordovician limestone aquifer, with average distances of 47.11 m, 96.59 m, 140.29 m, 161.03 m, and 176.12 m from the floor of the working face, respectively. The water pressure of the Ordovician limestone aquifer is 10–15 MPa. After regional grouting treatment, water inrush disasters from the coal seam floor in deep mining continue to occur frequently, which seriously restricts the safe production of the Xingdong coal mine.

3. Theoretical Analysis

3.1. Basic Principles. Based on the spatial semi-infinite body theory in elasticity [33] for the semi-infinite body bearing normal load or tangential load (Figure 3), the stress component of any point $M(x, y)$ can be expressed by Equations (1) and (2), respectively.

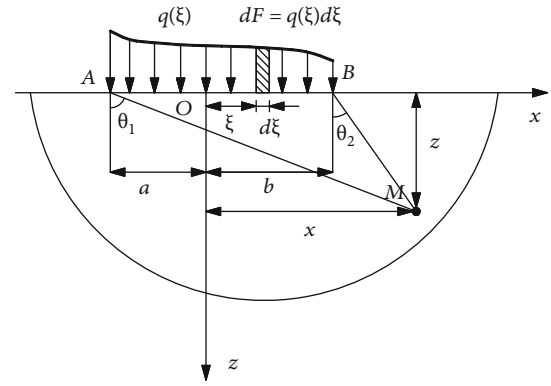

Figure 3: The mechanical models of a semi-infinite solid subjected to distributed load on the boundary.

$$\left.\begin{aligned}\sigma_z &= -\frac{2}{\pi}\int_{-a}^{b}\frac{\mathrm{q}(\xi)z^3d\xi}{\left[z^2+(x-\xi)^2\right]^2},\\ \sigma_x &= -\frac{2}{\pi}\int_{-a}^{b}\frac{q(\xi)z(x-\xi)^2d\xi}{\left[z^2+(x-\xi)^2\right]^2},\\ \tau_{zx} &= -\frac{2}{\pi}\int_{-a}^{b}\frac{q(\xi)z^2(x-\xi)d\xi}{\left[z^2+(x-\xi)^2\right]^2}.\end{aligned}\right\} \tag{1}$$

$$\left.\begin{aligned}\sigma_{sz} &= -\frac{2}{\pi}\int_{-a}^{b}\frac{q'(\xi)z^2(x-\xi)d\xi}{\left[z^2+(x-\xi)^2\right]^2},\\ \sigma_{sx} &= -\frac{2}{\pi}\int_{-a}^{b}\frac{q'(\xi)(x-\xi)^3d\xi}{\left[z^2+(x-\xi)^2\right]^2},\\ \tau_{szx} &= -\frac{2}{\pi}\int_{-a}^{b}\frac{q'(\xi)z(x-\xi)^2d\xi}{\left[z^2+(x-\xi)^2\right]^2}.\end{aligned}\right\} \tag{2}$$

Assuming that

$$\left.\begin{aligned}x-\xi &= \rho\sin\theta,\\ \mathrm{z}-\xi &= \rho\cos\theta,\\ d\xi &= \frac{\rho d\theta}{\cos\theta}.\end{aligned}\right\} \tag{3}$$

By substituting Equation (3) into Equations (1) and (2), the polar coordinate expression of vertical stress, horizontal stress, and shear stress can be obtained as shown in Equations (4) and (5).

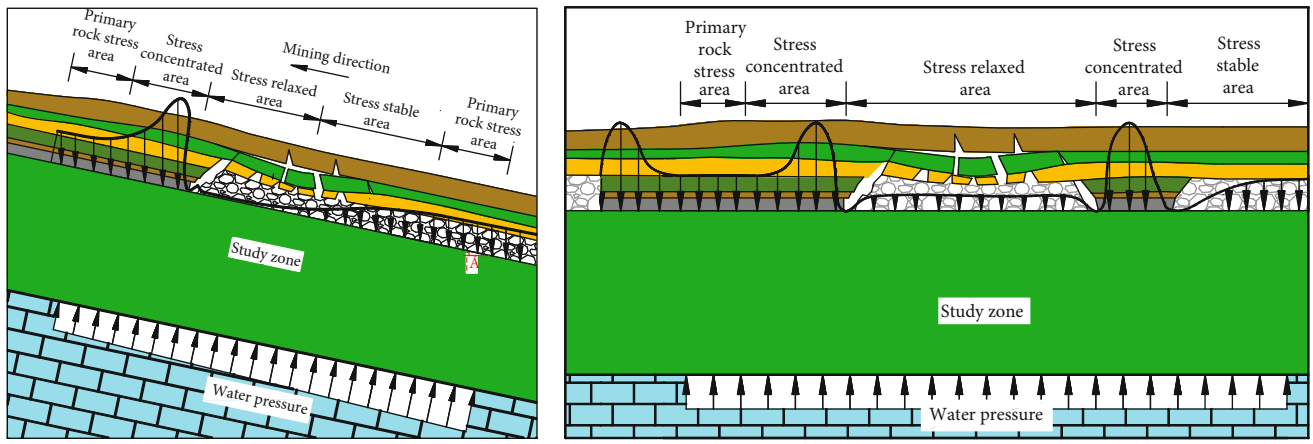

Figure 4: Schematic diagram of load on the floor under periodic weighting: (a) along the inclination; (b) along the strike.

$$\left.\begin{aligned}\sigma_z &= -\frac{2}{\pi}\int_{\theta_1}^{\theta_2} q(\xi)\cos^2\theta d\theta,\\ \sigma_x &= -\frac{2}{\pi}\int_{\theta_1}^{\theta_2} q(\xi)\sin^2\theta d\theta,\\ \tau_{zx} &= -\frac{2}{\pi}\int_{\theta_1}^{\theta_2} q(\xi)\sin\theta\cos\theta d\theta.\end{aligned}\right\} \quad (4)$$

$$\left.\begin{aligned}\sigma_{sz} &= -\frac{2}{\pi}\int_{\theta_1}^{\theta_2} q'(\xi)\sin\theta\cos\theta d\theta,\\ \sigma_{sx} &= -\frac{2}{\pi}\int_{\theta_1}^{\theta_2} q'(\xi)\frac{\sin^3\theta}{\cos\theta} d\theta,\\ \tau_{szx} &= -\frac{2}{\pi}\int_{\theta_1}^{\theta_2} q'(\xi)\sin^2\theta d\theta.\end{aligned}\right\} \quad (5)$$

3.2. Model Establishment. According to statistical analysis of floor water inrush disaster cases in deep mining, floor water inrush is frequently induced by strong mining pressure during periodic weighting [34, 35]. Therefore, it is of significant practical engineering to explore the redistribution of the floor stress and the floor failure range during periodic weighting [36]. Taking the longwall panel NO. 2129 at Xingdong coal mine as an example, the mining stress and the original rock stress are superimposed during the advancement of the working face. Figure 4 shows the general state of the floor rock mass of the island longwall panel in up-dip mining during periodic weighting based on the theory of ground pressure and strata control [37]. α is the dip angle of coal seam in Figure 4(a). Notably, compared with previous work, the dip angle of the mining direction and the goaf on both sides of the working face are considered, thereby enriching the investigation of floor stress and failure characteristics under different mining conditions.

Therefore, a mechanical model for the combination of the hydraulic pressure and mining pressure was constructed, as shown in Figure 5 and according to Figure 4. Both the mining pressure and the water pressure are simplified to a linear distribution in Figure 5. The water pressure is regarded as an uneven external force applied to the bottom of the aquifuge. In addition, the gravity of the floor strata is also considered. As shown in Figures 1 and 4(b), the width of coal pillar between longwall panels NO. 2129 and NO. 2222 is 74 m, and there is little effect of longwall panel NO. 2222 on the floor failure of longwall panel NO. 2129. Therefore, the stress in the mined area of longwall panel NO. 2222 is ignored in this paper.

In addition, the loads caused by the abutment pressure in Figure 5 are simplified to two triangular loads and decomposed accordingly into normal loads (q_1 and q_2) vertical to the floor and tangential loads (q_1' and q_2') parallel to the floor. The maximum value of them is determined by $(k_1 - 1)\gamma H\cos\alpha$. k_1 represents stress concentration coefficient, γ is the average bulk density of the overlying strata, and H denotes burial depth of coal seam. The floor stress in the mined zone is considered a uniformly distributed rectangular load q_0, which is released to the free surface with the magnitude of $-\gamma H\cos\alpha$. The stress recovery zone is gradually compacted by the overlying strata of the collapse zone, which is regarded as a triangular distribution load q_3 with the minimum value of $-\gamma H\cos\alpha$ and the maximum value of 0. Since floor failure is mainly affected by the stress increment, the component of the stress increment zone parallel to the floor is considered, ignoring the component of the stress in the unloading zone.

In Figure 5, L_1 is the length of the elastic zone caused by advanced abutment pressure, L_2 is the length of the plastic zone caused by advanced abutment pressure, L_3 is the length of the crushing zone induced by advanced abutment pressure, L_4 is the length of the stress recovery zone, L_5 is the

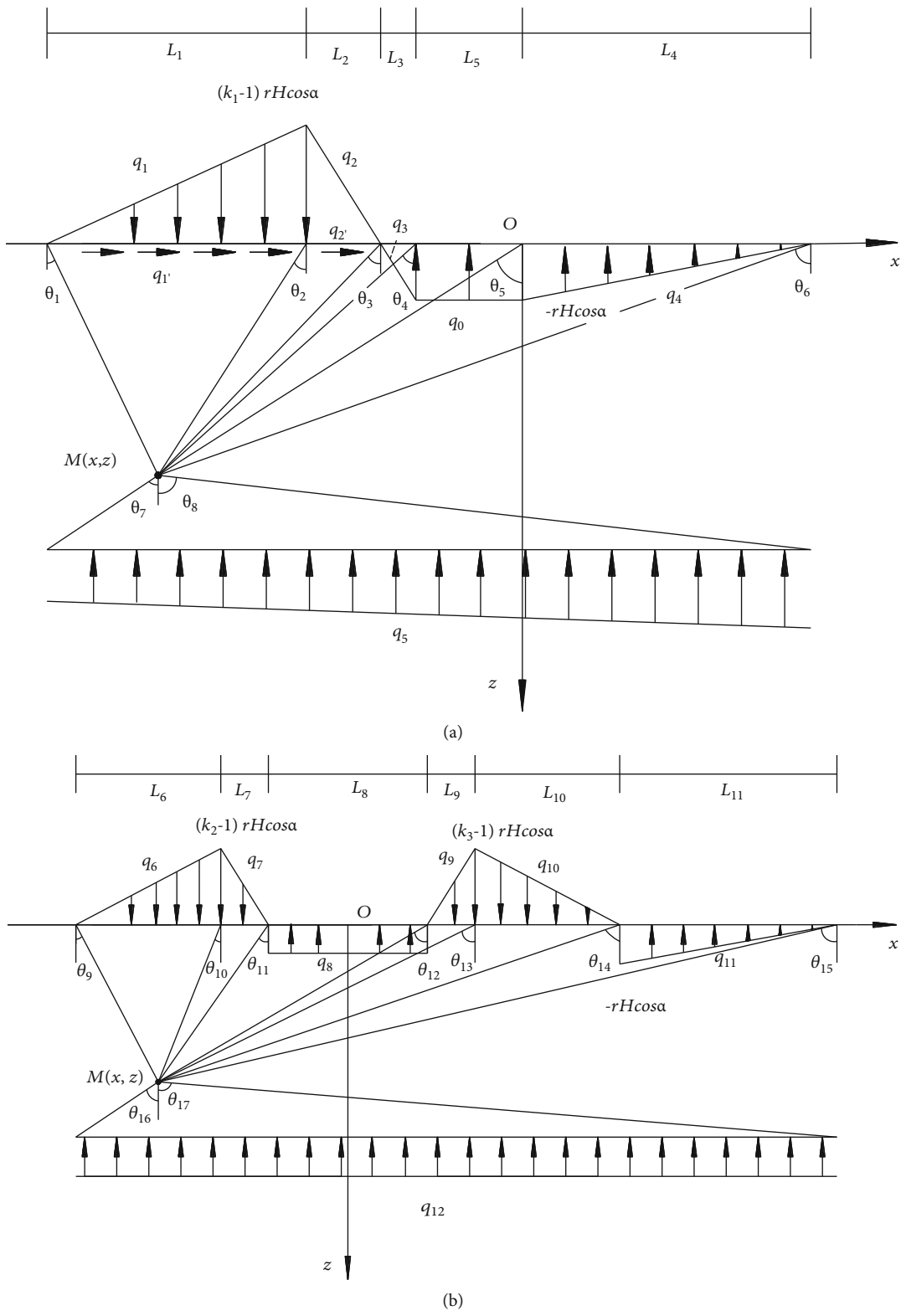

Figure 5: Mechanical models of floor stress in up-dip mining: (a) along the inclination; and (b) along the strike.

periodic weighting interval, L_6 and L_7 are the lengths of the plastic and elastic zones in the coal pillar along the strike, L_8 is the width of the working face, L_9 and L_{10} are the distances from the peak load point of the coal pillar to the boundary on both sides, and L_{11} is the distance of the stress recovery zone on the side of the isolated coal pillar.

The rock strata are assumed to be a continuous, intact, homogeneous, and an isotropic medium in the developed mechanical model, and the rock mass is assumed to apply the linear elastic constitutive model. According to the above assumptions, the stress components of M (x, z) can be derived by substituting the equations for all loads in Figure 5 into the corresponding Equations (4) and (5).

The calculation of stress components resulting from the triangular load q_1 are shown in Equation (6).

$$\left.\begin{aligned}
\sigma_{z1} &= \frac{(k_1-1)\gamma Hz\cos\alpha}{\pi L_1}\left[\tan\theta_1(\theta_1-\theta_2)-\frac{1}{2}\tan\theta_1\sin(2\theta_2)+\sin^2\theta_2\right],\\
\sigma_{x1} &= \frac{(k_1-1)\gamma Hz\cos\alpha}{\pi L_1}\left[\tan\theta_1(\theta_1-\theta_2)+\tan\theta_1\sin\theta_2\cos\theta_2+2\ln\frac{\cos\theta_1}{\cos\theta_2}-\sin^2\theta_2\right],\\
\tau_{zx1} &= \frac{(k_1-1)\gamma Hz\cos\alpha}{\pi L_1}\left[\tan\theta_1\left(\sin^2\theta_1-\sin^2\theta_2\right)+(\theta_2-\theta_1)+\frac{1}{2}\left(\sin(2\theta_1)-\sin(2\theta_2)\right)\right].
\end{aligned}\right\} \tag{6}$$

As regards the stress components induced by the triangular load q_2, θ_1 and θ_2 in Equation (6) should be replaced by θ_3 and θ_2, respectively, and the corresponding distance by L_2. Similarly, the corresponding stress components for the triangular loads q_3, q_4,q_6,q_7,q_9,q_{10}, and q_{11} can be obtained.

The calculation of stress components resulting from the triangular load q_0 are shown in Equation (7).

$$\left.\begin{aligned}
\sigma_{z0} &= \frac{-\gamma H}{\pi}\left(\theta_4-\theta_5+\frac{1}{2}\sin 2\theta_4-\frac{1}{2}\sin 2\theta_5\right),\\
\sigma_{x0} &= \frac{-\gamma H}{\pi}\left[\theta_4-\theta_5-\frac{1}{2}\sin 2\theta_4+\frac{1}{2}\sin 2\theta_5\right],\\
\tau_{zx0} &= \frac{-\gamma H}{\pi}(\cos 2\theta_5-\cos 2\theta_4).
\end{aligned}\right\} \tag{7}$$

For the stress component induced by the rectangular load q_8, θ_4 and θ_5 in Equation (7) should be replaced by θ_{11} and θ_{12}, respectively. Similarly, the corresponding stress component for the rectangular load q_{12} can be obtained.

Equation (8) calculate the stress components caused by the load q_5.

$$\left.\begin{aligned}
\sigma_{z5} &= \frac{(H_z-z)\rho_w g\sin\alpha}{\pi}\left[\tan\theta_7(\theta_8-\theta_7)+\frac{1}{2}\tan\theta_7\sin(2\theta_8)-\sin^2\theta_8\right]\\
&+\frac{P_0}{\pi}\left(\theta_7-\theta_8+\frac{1}{2}\sin 2\theta_7-\frac{1}{2}\sin 2\theta_8\right),\\
\sigma_{x5} &= \frac{(H_z-z)\rho_w g\sin\alpha}{\pi}\left[\tan\theta_7(\theta_8-\theta_7)-\tan\theta_8\sin\theta_7\cos\theta_7-2\ln\frac{\cos\theta_8}{\cos\theta_7}+\sin^2\theta_8\right]\\
&+\frac{P_0}{\pi}\left[\theta_7-\theta_8-\frac{1}{2}\sin 2\theta_7+\frac{1}{2}\sin 2\theta_8\right],\\
\tau_{zx5} &= \frac{(H_z-z)\rho_w g\sin\alpha}{\pi}\left[\tan\theta_7\left(\sin^2\theta_8-\sin^2\theta_7\right)-(\theta_8-\theta_7)-\frac{1}{2}\left(\sin(2\theta_7)-\sin(2\theta_8)\right)\right]\\
&+\frac{P_0}{\pi}(\cos 2\theta_8-\cos 2\theta_7).
\end{aligned}\right\} \tag{8}$$

The stress components caused by the load $q_1{}'$ can be obtained using Equation (9).

$$\left.\begin{aligned}
\sigma_{sz1} &= \frac{(k_1-1)\gamma Hz\sin\alpha}{\pi L_1}\left[\tan\theta_1\left(\sin^2\theta_2-\sin^2\theta_1\right)+\theta_1-\theta_2-\frac{1}{2}\left(\sin 2\theta_1-\sin 2\theta_2\right)\right],\\
\sigma_{sx1} &= \frac{(k_1-1)\gamma Hz\sin\alpha}{\pi L_1}\left[\tan\theta_1\left(\sin^2\theta_1-\sin^2\theta_2-2\ln\frac{\cos\theta_2}{\cos\theta_1}\right)+3(\theta_2-\theta_1)-2(\tan\theta_2-\tan\theta_1)-\frac{1}{2}\left(\sin 2\theta_2-\sin 2\theta_1\right)\right],\\
\tau_{szx1} &= \frac{(k_1-1)\gamma Hz\sin\alpha}{\pi L_1}\left\{\sin^2\theta_2-\sin^2\theta_1-2\ln\frac{\cos\theta_1}{\cos\theta_2}-\tan\theta_1\left[\theta_1-\theta_2-\frac{1}{2}\left(\sin 2\theta_2-\sin 2\theta_1\right)\right]\right\}.
\end{aligned}\right\} \tag{9}$$

For the stress component induced by the load $q_2{}'$, θ_1 and θ_2 in Equation (9) should be replaced by θ_3 and θ_2, respectively.

In Equations (6)–(9), H is the burial depth of the coal seam, α is the dip angle of the coal seam, k_1 is the concentration coefficient of advance abutment pressure, k_2 and k_3 are the concentration coefficient of abutment pressure on coal pillar at both ends of working face along the strike, γ indicates bulk density of the rock mass, ρ_w is density of confined water, P_0 denotes the hydraulic pressure of the confined aquifer, g is gravitational acceleration, and H_z is the distance between the coal seam floor and confined aquifer.

The angle in the above Equation can be calculated according to Equation (10).

$$\left.\begin{aligned}
\theta_1 &= \arctan\frac{x+L_1+L_2+L_3+L_5}{z},\\
\theta_2 &= \arctan\frac{x+L_2+L_3+L_5}{z},\\
\theta_3 &= \arctan\frac{x+L_3+L_5}{z},\\
\theta_4 &= \arctan\frac{x+L_5}{z},\\
\theta_5 &= \arctan\frac{x}{z},\\
\theta_6 &= \arctan\frac{x-L_4}{z},\\
\theta_7 &= \arctan\frac{x+L_1+L_2+L_3+L_5}{H_z-z},\\
\theta_8 &= \arctan\frac{x-L_4}{H_z-z},\\
\theta_9 &= \arctan\frac{x+L_6+L_7+1/2L_8}{z},\\
\theta_{10} &= \arctan\frac{x+L_7+1/2L_8}{z},\\
\theta_{11} &= \arctan\frac{x+1/2L_8}{z},\\
\theta_{12} &= \arctan\frac{x-1/2L_8}{z},\\
\theta_{13} &= \arctan\frac{x-1/2L_8-L_9}{z},\\
\theta_{14} &= \arctan\frac{x-1/2L_8-L_9-L_{10}}{z},\\
\theta_{15} &= \arctan\frac{x-1/2L_8-L_9-L_{10}-L_{11}}{z},\\
\theta_{16} &= \arctan\frac{x+L_6+L_7+1/2L_8}{H_z-z},\\
\theta_{17} &= \arctan\frac{x-1/2L_8-L_9-L_{10}-L_{11}}{H_z-z}.
\end{aligned}\right\} \tag{10}$$

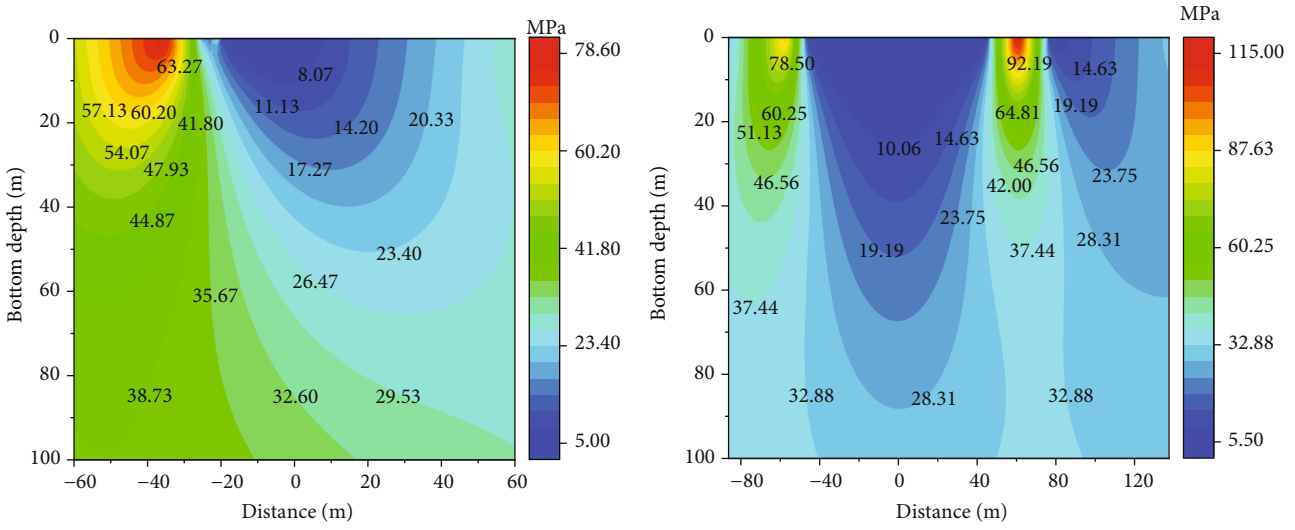

Figure 6: The isoline of the vertical stress: (a) along the inclination; and (b) along the strike.

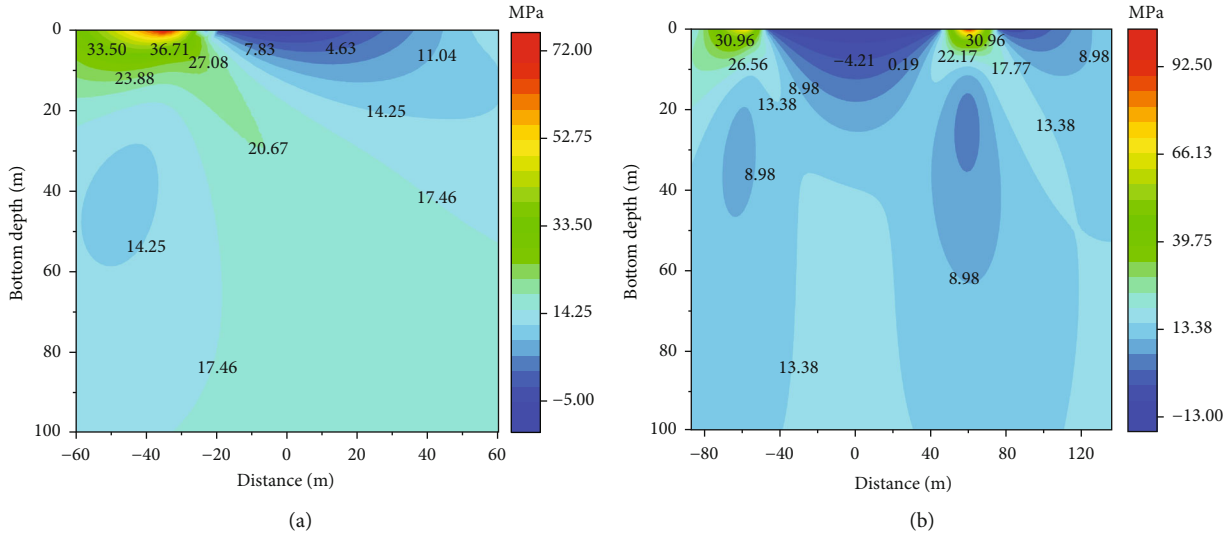

Figure 7: The isoline of the horizontal stress: (a) along the inclination; and (b) along the strike.

3.3. Redistribution Law of Floor Stress. The total stress of M (x, z) in the floor can be obtained by summing the stress components induced by the abutment pressure, water pressure, and ground stress. According to the principle of stress superposition in elasticity theory, the vertical, horizontal, and shear stress at a point M (x, z) in the floor when the periodic weighting can be calculated as follows.

$$\left.\begin{aligned}\sigma_z &= \sigma_{z1} + \sigma_{sz1} + \sigma_{z2} + \sigma_{sz2} + \sigma_{z3} + \sigma_{z0} + \sigma_{z4} + \sigma_{z5} + \gamma(H+z),\\ \sigma_x &= \sigma_{x1} + \sigma_{sx1} + \sigma_{x2} + \sigma_{sx2} + \sigma_{x3} + \sigma_{x0} + \sigma_{x4} + \sigma_{x5} + \lambda\gamma(H+z),\\ \tau_{zx} &= \tau_{zx1} + \tau_{szx1} + \tau_{zx2} + \tau_{szx2} + \tau_{zx3} + \tau_{zx0} + \tau_{zx4} + \tau_{zx5}.\end{aligned}\right\} \tag{11}$$

$$\left.\begin{aligned}\sigma_x &= \sigma_{x6} + \sigma_{x7} + \sigma_{x8} + \sigma_{x9} + \sigma_{x10} + \sigma_{x11} + \sigma_{x12} + \gamma(H+z),\\ \sigma_z &= \sigma_{z6} + \sigma_{z7} + \sigma_{z8} + \sigma_{z9} + \sigma_{z10} + \sigma_{z11} + \sigma_{z12} + \lambda\gamma(H+z),\\ \tau_{zx} &= \tau_{zx6} + \tau_{szx7} + \tau_{zx8} + \tau_{szx9} + \tau_{zx10} + \tau_{zx11} + \tau_{zx12}.\end{aligned}\right\} \tag{12}$$

Where Equation (11) is the total stress component of the floor stress along the inclination and Equation (12) is the total stress component of the floor stress along the strike.

According to the site investigation, it is found that the roof of the coal seam #2 at Xingdong coal mine is difficult to cave in time, with a larger overhanging roof distance, which leads to a larger weighting interval, and the concentration degree of nearby abutment pressure will increase,

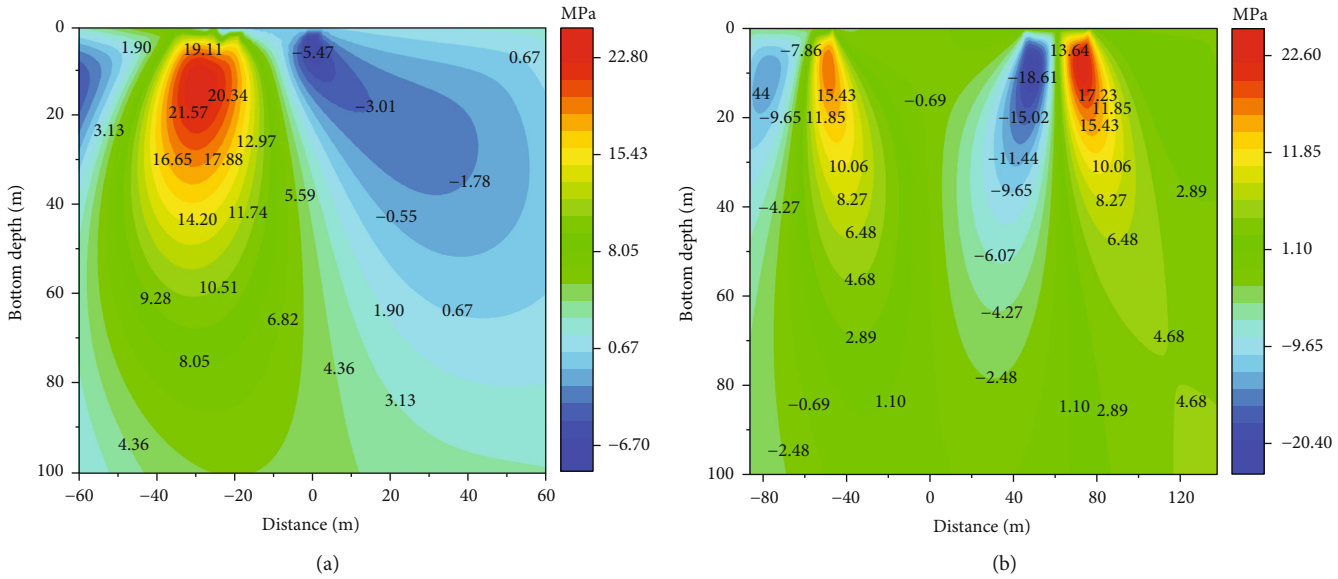

Figure 8: The isoline of the shear stress: (a) along the inclination; and (b) along the strike.

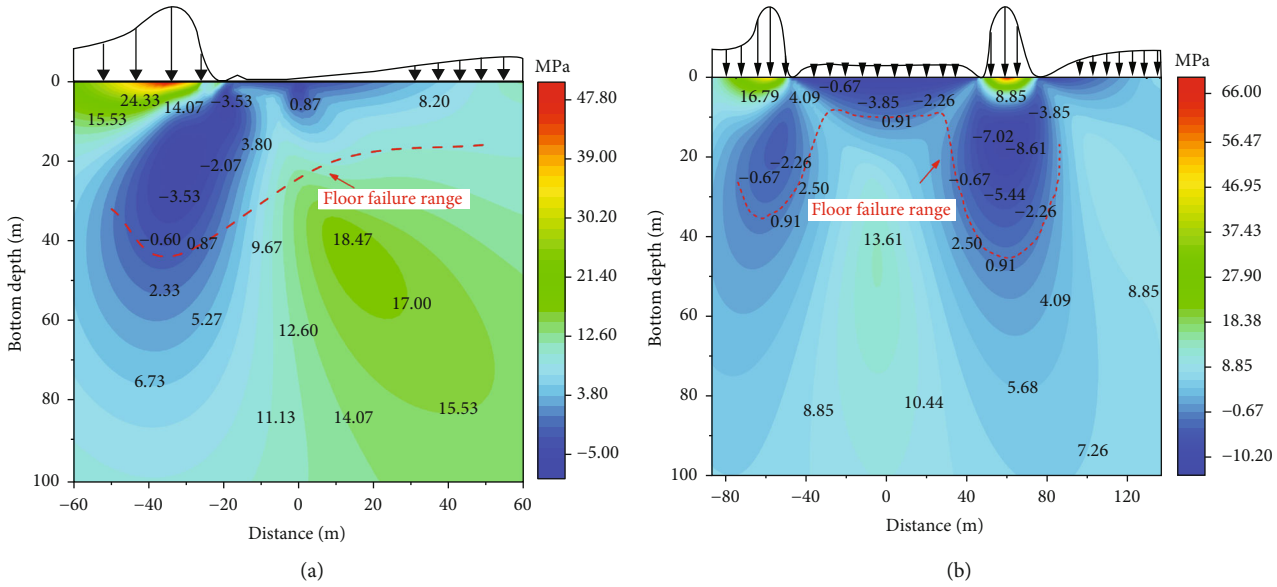

Figure 9: The floor failure zones: (a) along the inclination; and (b) along the strike.

especially when the stress concentration factor below the isolated coal pillar will be greater.

According to the geological survey report and field monitoring data of the longwall panel NO. 2129 at Xingdong coal mine, $L_1 = 50$ m, $L_2 = 10$ m, $L_3 = 5$ m, $L_4 = 60$ m, $L_5 = 20$ m, $L_6 = 30$ m, $L_7 = 10$ m, $L_8 = 92.5$ m, $L_9 = 15$ m, $L_{10} = 15$ m, $L_{11} = 60$ m, $k_1 = 3.5$, $k_2 = 2.5$, $k_2 = 3.5$, $P_0 = 10$ MPa, $\gamma = 25$ kN/m^3, $\rho_w = 1000$ kg/m^3, $g = 10$ N/kg, $H_z = 180$ m, $\alpha = 11°$, and $H = 1000$ m. Substituting the above parameters into Equation (12), the floor stress component isoline under the combination of mining stress and water pressure can be obtained by using Python programming.

The vertical stress concentration is observed in the floor underlying the advanced abutment pressure zone along the inclination (Figure 6(a)). The maximum value of stress concentration is near the elastic-plastic bond of the coal seam, that is, near the peak of the advanced abutment pressure. The stress unloading zone is mainly located in the mined area, as well as the maximum degree of stress relief within the weighting interval (L_5). Along the strike direction, the vertical stress concentration in the floor below the isolated coal pillar due to the overhanging roof of the coal seam after mining is greater than that in other areas (Figure 6(b)).

Figure 7 shows that the variation of the horizontal stress is consistent with the distribution of the vertical stress. The degree of concentration and unloading and influence range of horizontal stress are significantly smaller than those of vertical stress. The influence range of horizontal stress

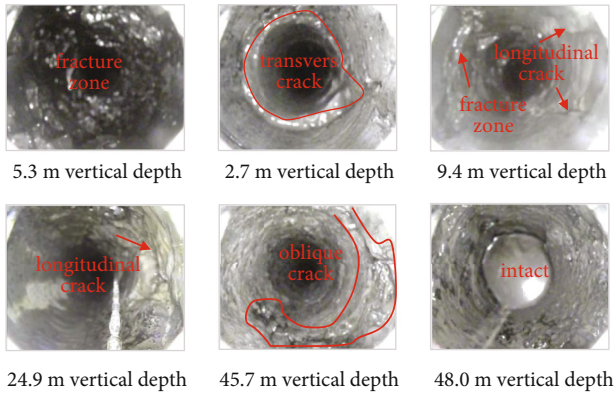

Figure 10: Floor failure depth measurement without RHF.

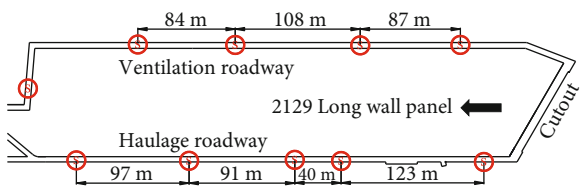

Figure 11: Layout of microseismic monitoring stations.

decreases rapidly as the depth increases. However, tensile stress is generated in the unloading zone along the inclination and along the strike.

The shear stress in the mined zone and the coal wall approximately presents a positive and a negative shear force couple along the inclination, forming a sharp shear stress variation zone (Figure 8(a)). The floor strata of this area are prone to compression shear or tension shear deformation damage, which is consistent with the vulnerable location around the stope on site. The maximum shear stress appears at the coal wall zones affected by advanced abutment pressure. The shear stress along the strike is also a positive and negative shear couple in the floor strata under the mined zones and the coal pillars, while the maximum shear stress appears on the side of the isolated coal pillar (Figure 8(b)).

3.4. Failure Characteristics of Floor Strata. Based on the Mohr-Coulomb failure criterion [38], the rock mass will be damaged when the maximum shear stress at a point in the floor rock strata equals or exceeds its shear strength. Equation (13) calculates the condition for shear failure to occur in the floor [17].

$$\frac{(\sigma_z + \sigma_x/2)\tan\varphi + c}{\sqrt{1+\tan^2\varphi}} \le \tau_{\max}, \tag{13}$$

where the maximum shear stress $\tau_{\max}$ is calculated as follows:

$$\tau_{\max} = \sqrt{{\tau_z}^2 + \left(\frac{\sigma_z - \sigma_x}{2}\right)^2}, \tag{14}$$

Substituting Equation (15) into Equation (13), we can construct the floor failure criterion Equation (15).

$$\mathrm{F}(x,z) = \frac{(\sigma_z + \sigma_x/2)\tan\varphi + c}{\sqrt{1+\tan^2\varphi}} - \sqrt{{\tau_z}^2 + \left(\frac{\sigma_z - \sigma_x}{2}\right)^2}, \tag{15}$$

where c and φ denote the cohesion and internal friction angle of the floor rock mass, respectively.

When $F(x, z) \le 0$, the floor strata fails. According to the laboratory test results, the weighted average method is used to determine the average friction angle $\varphi = 35.4^\circ$ and cohesive force $c = 4$ MPa and substituting into Equation (15). The $F(x, z)$ contour is obtained by using Python programming to calculate the theoretical floor failure characteristics of the island longwall panel in up-dip mining above confined aquifer during periodic weighting, as shown in Figure 9.

As seen in Figure 9(a), the floor failure characteristic along the inclination is spoon-shaped. Under the effect of advanced abutment pressure and high-water pressure, the maximum depth of floor failure reaches 43.2 m. The location of the maximum failure depth is in the floor of the stress concentration area of the coal wall in front of the working face. Tensile failure occurs within 10 m below the mined zone, resulting in floor heave. Shear failure occurs in the range of 10 m–43.2 m below the mined zone. With the increase of the floor failure depth, high-pressure confined water can easily rise from the shear failure zone to the bottom of the aquifuge, resulting in water inrush accidents.

Figure 9(b) shows that the floor failure range along the strike has an "asymmetric saddle shape." The maximum failure depth of the floor is 45.1 m, which is located on the side of the isolated coal pillar. Due to the abutment pressure of the two working faces on the side of the isolated coal pillar, the stress concentration factor increases, resulting in a large floor failure depth, and floor water inrush is likely to occur.

4. In Situ Measurement

To verify the feasibility of theoretical analysis, the borehole televiewer (BTV) and microseismic monitoring were used to detect the floor failure characteristics of the island longwall panel NO. 2129 before and after RHF.

4.1. Results of Borehole Televiewer Detection before RHF. The BTV is an effective means to visually analyze the failure range of the surrounding rock [39]. The evolution of internal fractures in the surrounding rock can be observed by a digital borehole television [40], which helps to determine the depth and range of fracture development induced by mining [41]. Therefore, to investigate the floor borehole, we examined the distribution of fractures in the sidewalls of the borehole by using a BTV (Figure 10). A CXK12(A) of BTV is equipped with a wide-viewing panoramic color camera with 1.34 million pixels, which can resolve cracks of 0.1 mm. According to the detection results, the floor fracture development demarcation point can be observed. The BTV image shows that the cracks are densely developed 0–45.7 m away from the borehole wall (Figure 10), but no cracks exceed this

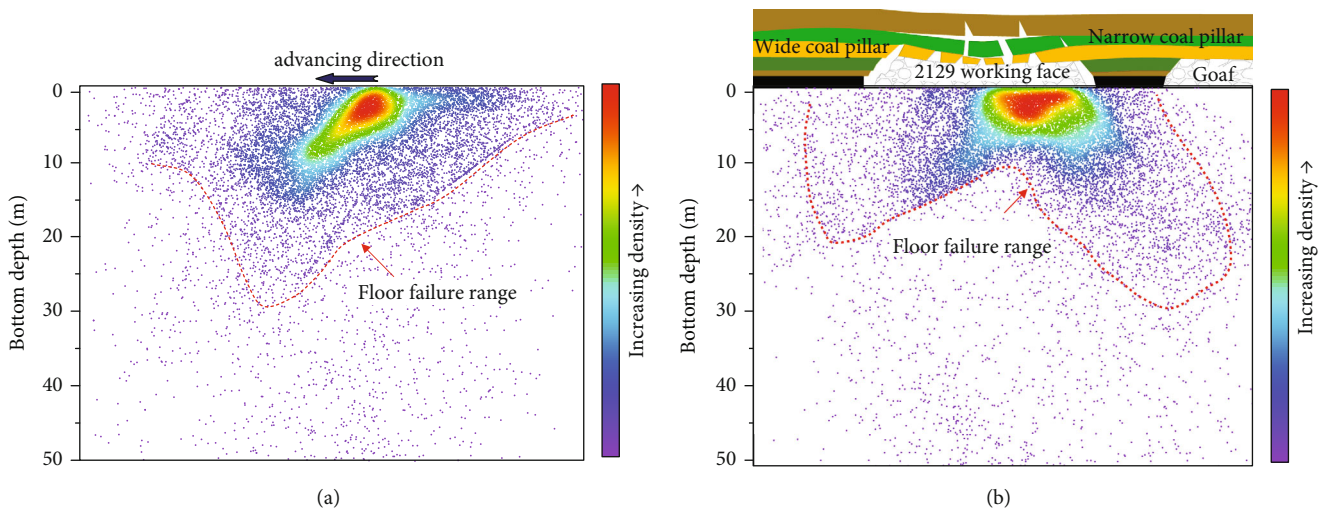

Figure 12: Microseismic monitoring results of floor failure range after RHF: (a) along the inclination; and (b) along the strike.

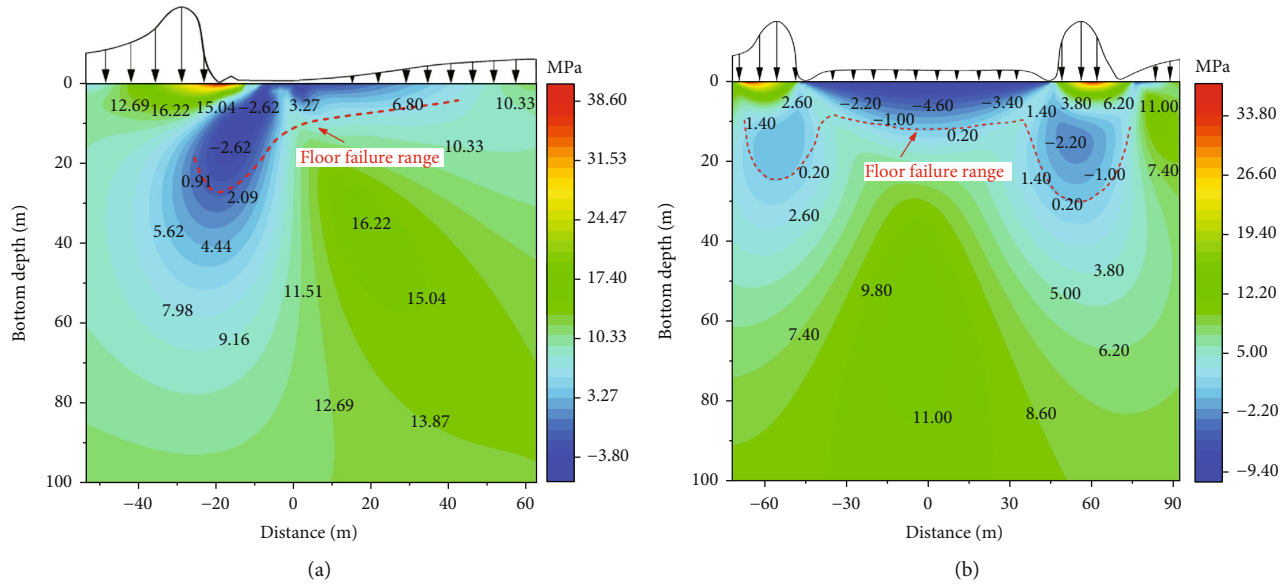

Figure 13: Theoretical calculation results of floor failure range after RHF: (a) along the inclination; and (b) along the strike.

area. The mining failure depth of the floor is 45.7 m, and the mining failure fractures will be connected with the Yeqing aquifer (47.1 m away from the coal seam floor on average).

According to theoretical calculations, the maximum failure depth of the floor before roof fracturing in the longwall panel NO. 2129 of the Xingdong coal mine is 45.1 m. The theoretical calculation results are consistent with the measurements taken from the site, indicating that the establishment of a mechanical model can accurately predict the floor failure depth. Under the superposition of high-water pressure and mining stress, the floor failure zone under the isolated coal pillar on one side of the island longwall panel easily connects with the Yeqing aquifer. The Yeqing aquifer is connected with Ordovician limestone through longitudinal water conducting fissures or structures, which can easily cause floor water inrush. Therefore, RHF is performed on site to break the hard roof of the working face and isolated coal pillar in advance to reduce the mining pressure and decrease the floor failure depth.

4.2. Results of Microseismic Monitoring after RHF. The formation process of the water conducting channels and the damage degree of the surrounding rock can be determined by using microseismic events [5, 26–28]. To monitor the development range of mining fractures in the floor after RHF, a microseismic monitoring system was installed in the roadway of the longwall panel NO. 2129 (Figure 11). A total of 10 microseismic sensors were installed in the ventilation roadway and haulage roadway, and the microseismic events were transmitted to the data processing center in real time through the collection substation. The sensors are ESG (Engineering Seismology Group) detectors. Three collection substations were installed with a sampling frequency of 5 kHz.

Figure 12 shows the distribution of microseismic monitoring events after roof fracturing. The abscissa is the position of the working face, and the ordinate is the depth of the coal seam floor. Figure 12(a) shows that the microseismic events in the floor are concentrated within 15 m of the floor, indicating that the shallow floor rock mass is first damaged under the action of mining stress. With increasing floor depth, the density of floor microseismic events decreases gradually. The distribution shape of the microseismic event density in the floor is a "spoon-shaped" along the advancing direction of the working face. According to the microseismic monitoring results, the maximum mining failure depth is 28.6 m (Figure 12(a)). Microseismic events are mainly concentrated on the floor of the goaf at the side of the isolated coal pillar along the strike. The floor failure range is also an "asymmetric inverted saddle-shaped," and the maximum failure depth is 29.1 m, located on the side of the isolated coal pillar (Figure 12(b)). No water inrush accident occurred during mining. The maximum floor failure depth of the working face along the strike or the inclined direction decreased significantly after RHF. The hard rock strata fractured and collapsed reducing the stress concentration in the isolated coal pillar and working face after hydraulic fracturing of roof.

The relevant parameters after RHF in the island longwall panel NO. 2129 are substituted into the theoretical model to obtain the corresponding floor failure characteristics. According to the on-site monitoring results, the measured values of various parameters after roof fracturing are $L_1 = 35\,\text{m}$, $L_2 = 7\,\text{m}$, $L_3 = 3\,\text{m}$, $L_4 = 60\,\text{m}$, $L_5 = 10\,\text{m}$, $L_6 = 20\,\text{m}$, $L_7 = 5\,\text{m}$, $L_8 = 92.5\,\text{m}$, $L_9 = 15\,\text{m}$, $L_{10} = 15\,\text{m}$, $L_{11} = 15\,\text{m}$, $k_1 = 2.5$, $k_2 = 1.5$, $k_2 = 1.5$, $P_0 = 10\,\text{MPa}$, $\gamma = 25\,\text{kN/m}^3$, $\rho_w = 1000\,\text{kg/m}^3$, $g = 10\,\text{N/kg}$, $H_z = 180\,\text{m}$, $\alpha = 11^\circ$, $H = 1000\,\text{m}$, $\varphi = 35.4^\circ$, and $c = 4\,\text{MPa}$. Substituting the above parameters into Equation (15), the floor failure depths along the inclination and the strike are 25.6 m and 29.9 m, respectively. The theoretical prediction values of the maximum failure depth and failure characteristics after roof fracturing are consistent with the microseismic monitoring results (Figure 13), indicating the feasibility and applicability of the theoretical model. The theoretical calculation results can provide a reference for the failure depth of the floor before mining.

5. Conclusion

A two-dimensional hydraulic calculation model was proposed to analyze the floor failure characteristics in deep island longwall panel using the up-dip mining method. The effects of mining stress and confined water pressure in the calculation model was considered in this paper. The floor failure depth and failure characteristics before and after RHF were discussed in association with the BTV and microseismic monitoring system, verifying the theoretical model. The main conclusions in this paper are as follows:

(1) The vertical stress in the floor is principally concentrated in the rock strata advanced the working face and under the coal pillar. The degree of concentration and unloading of the vertical stress are significantly greater than those of the horizontal stress. The shear stress distribution is approximately the coupling of positive and negative. Along the working face advance direction, the local stress concentration on the side of the coal pillar, and stress release on the side of the mined zone are observed. The stress concentration under the coal pillar is greater than that in other zones along the strike due to the stress superposition on the coal pillar

(2) The maximum floor failure depth before RHF is theoretically calculated to be 45.1 m, which is consistent with the 45.7 m depth detected by BTV. The theoretical calculation result of the floor failure depth after roof fracturing is 29.9 m, which is approximately equal to the microseismic monitoring result of 29.1 m

(3) The theoretical failure characteristics of the island longwall panel in up-dip mining along the inclination and the strike are approximately "spoon-shaped" and "asymmetric inverted saddle-shaped," respectively. The theoretical calculation of the floor failure characteristics and failure depth before and after roof fracturing are consistent with the measured on-site results, which verifies the rationality of the theoretical model

Data Availability

The data that support the findings of this study are available from the corresponding author upon reasonable request.

Conflicts of Interest

The authors declare that they have no known competing financial interests or personal relationships that could have appeared to influence the work reported in this paper.

Acknowledgments

This work was supported by the National Natural Science Foundation of China (Nos. U1910206, 51874312, and 51861145403), the Science and Technology Plant Project of Inner Mongolia Autonomous Region (No. 2019GG140), the Major Scientific and Technological Innovation Project of Shandong Province (No. 2019SDZY01), the Beijing Municipal Natural Science Foundation (No. 8184082), the Scientific and Technological Support Project of Guizhou Province: Qiankehe Support (2021) general 353, and the Scientific and Technological Support Project of Guizhou Province: Qiankehe Support (2021) general 514.

References

[1] C. Li, J. Zuo, Y. Shi et al., "Deformation and fracture at floor area and the correlation with main roof breakage in deep longwall mining," *Natural Hazards*, vol. 107, no. 2, pp. 1731–1755, 2021.

[2] W. Liu, D. Mu, X. Xie, L. Yang, and D. Wang, "Sensitivity analysis of the main factors controlling floor failure depth and a

risk evaluation of floor water inrush for an inclined coal seam," *Mine Water and the Environment*, vol. 37, no. 3, pp. 636–648, 2018.

[3] A. Vervoort, "Various phases in surface movements linked to deep coal longwall mining: from start-up till the period after closure.," *International Journal of Coal Science and Technology*, vol. 8, no. 3, pp. 412–426, 2021.

[4] S. Dong, H. Wang, X. Guo, and Z. Zhou, "Characteristics of water hazards in China's coal mines: a review," *Mine Water and the Environment*, vol. 40, no. 2, pp. 325–333, 2021.

[5] K. Ma, X. Y. Sun, C. A. Tang, F. Z. Yuan, S. J. Wang, and T. Chen, "Floor water inrush analysis based on mechanical failure characters and microseismic monitoring," *Tunnelling and Underground Space Technology*, vol. 108, article 103698, 2021.

[6] S. Dong, W. Zhang, W. Zhou et al., "Discussion on some topical issues of water prevention and control in coal mines," *Mine Water and the Environment*, vol. 40, no. 2, pp. 547–552, 2021.

[7] J. Zhang, "Investigations of water inrushes from aquifers under coal seams," *International Journal of Rock Mechanics and Mining Sciences*, vol. 42, no. 3, pp. 350–360, 2005.

[8] S. Zhu, Z. Jiang, K. Zhou, G. Peng, and C. Yang, "The characteristics of deformation and failure of coal seam floor due to mining in Xinmi coal field in China," *Bulletin of Engineering Geology and the Environment*, vol. 73, no. 4, pp. 1151–1163, 2014.

[9] S. Liu, W. Liu, and J. Shen, "Stress evolution law and failure characteristics of mining floor rock mass above confined water," *KSCE Journal of Civil Engineering*, vol. 21, no. 7, pp. 2665–2672, 2017.

[10] X. Meng, C. Xu, Z. Gao, and X. Wang, "Stress distribution and damage mechanism of mining floor," *Journal of China Coal Society*, vol. 35, no. 11, pp. 1832–1836, 2010.

[11] H. Zhang and L. Wang, "Journal of mining and safety engineering," *Journal of Mining and Safety Engineering*, vol. 28, no. 2, 2011.

[12] W. Xue et al., "Theoretical analysis and field measurement of floor failure in gob side entry of cutting roof in confined water mine area," *Journal of China Coal Society*, pp. 1–9, 2020.

[13] R. Yang, Y. Zhu, Y. Li, and W. Li, "Stress distribution and damage characteristics of roadway floor in layered rock mass," *Journal of China University of Mining and Technology*, vol. 49, no. 4, 2020.

[14] R. Yang, Y. Zhu, Y. Li, W. Li, and B. Xiao, "Stability analysis and control strategy of weakly cemented layered floor in mining affected roadway," *Journal China Coal Soc.*, vol. 45, no. 7, pp. 2667–2680, 2020.

[15] H. Lu, D. Yao, Y. Hu, and J. Sun, "Elasticity solution for failure depth of mining floor under water pressure," *Journal of Mining & Safety Engineering*, vol. 34, no. 3, pp. 452–458, 2017.

[16] C. Zhao, "Microseismic test and numerical simulation analysis of floor failure depth of isolated coal mining face," *Coal Geology and Exploration*, vol. 47, no. 4, pp. 110–116, 2019.

[17] J. Sun, L. Wang, and G. Zhao, "Stress distribution and failure characteristics for workface floor of a tilted coal seam," *KSCE Journal of Civil Engineering*, vol. 23, no. 9, pp. 3793–3806, 2019.

[18] W. Liu, D. Mu, X. Xie, W. Zhang, and D. Yuan, "Rules of stress distributions and failure characteristics in inclined coal seam floor due to mining," *Journal of Mining & Safety Engineering*, vol. 35, no. 4, pp. 756–764, 2018.

[19] W. Liu, J. Shen, and H. Jia, "Mining-induced stress evolution law and failure characteristics of floor in deep mine," *Journal of Mining & Safety Engineering*, vol. 33, no. 6, pp. 1045–1051, 2016.

[20] W. Song, Z. Liang, and C. Zhao, "Mechanical failure characteristics of mining floor along working face inclination above confined water," *Chinese Journal of Rock Mechanics and Engineering*, vol. 37, no. 9, pp. 2131–2143, 2018.

[21] Z. Liang, W. Song, and W. Liu, "Theoretical models for simulating the failure range and stability of inclined floor strata induced by mining and hydraulic pressure," *International Journal of Rock Mechanics and Mining Sciences*, vol. 132, article 104382, 2020.

[22] J. Chen, X. Zuqiang, and L. Hui, "Failure characteristics of floor under predssure inclined and extra thick coal seam in full-mechanized top coal caving faces," *Chinese Journal of Rock Mechanics and Engineering*, vol. 35, pp. 3018–3023, 2016.

[23] Y. Chen, S. Zhu, Z. Wang, and F. Li, "Deformation and failure of floor in mine with soft coal, soft floor, hard roof and varying thicknesses of coal seam," *Engineering Failure Analysis*, vol. 115, article 104653, 2020.

[24] H. Liu, P. Wang, W. Zhang, Q. Liu, and L. Su, "Comprehensive measurement of the deformation and failure of floor rocks: a case study of the Xinglongzhuang coal mine," *Geofluids*, vol. 2020, 14 pages, 2020.

[25] Y. Hu, W. Li, S. Liu, and Q. Wang, "Prediction of floor failure depth in deep coal mines by regression analysis of the multifactor influence index," *Mine Water and the Environment*, vol. 40, no. 2, pp. 497–509, 2021.

[26] G. Cheng, C. Tang, L. Li, X. Chuai, T. Yang, and L. Wei, "Micro-fracture precursors of water flow channels induced by coal mining: a case study," *Mine Water and the Environment*, vol. 40, no. 2, pp. 398–414, 2021.

[27] Y. Zhao, T. Yang, P. Zhang, H. Xu, and S. Wang, "Inversion of seepage channels based on mining-induced microseismic data," *International Journal of Rock Mechanics and Mining Sciences*, vol. 126, article 104180, 2020.

[28] J. R. Zhou, T. H. Yang, P. H. Zhang, T. Xu, and J. Wei, "Formation process and mechanism of seepage channels around grout curtain from microseismic monitoring: a case study of Zhangmatun iron mine, China," *Engineering Geology*, vol. 226, pp. 301–315, 2017.

[29] A. P. Cheng, Y. T. Gao, C. Liu, and J. F. Chai, "Microseismic monitoring and numerical simulation research of floor failure depth in extra-thick coal seam," *Advances in Materials Research*, vol. 881-883, pp. 1799–1804, 2014.

[30] S. Luo, Y. Wu, H. Wang, and P. Xie, "Asymmetric failure pattern and slip characteristics of floor of longwall face in steeply dipping seam mining," *Journal of China Coal Society*, vol. 43, no. 8, pp. 2155–2161, 2018.

[31] Y. Jiang, H. Wang, S. Xue, Y. Zhao, J. Zhu, and X. Pang, "Assessment and mitigation of coal bump risk during extraction of an island longwall panel," *International Journal of Coal Geology*, vol. 95, pp. 20–33, 2012.

[32] S. Zhu, Y. Feng, F. Jiang, and J. Liu, "Mechanism and risk assessment of overall-instability-induced rockbursts in deep island longwall panels," *International Journal of Rock Mechanics and Mining Sciences*, vol. 106, pp. 342–349, 2018.

[33] Z. Xu, *Concise Tutorial on Elasticity*, Higher Education Press, Beijing, China, 2002.

[34] E. Eberhardt, B. Stimpson, and D. Stead, "Effects of grain size on the initiation and propagation thresholds of stress-induced brittle fractures," *Rock Mechanics and Rock Engineering*, vol. 32, no. 2, pp. 81–99, 1999.

[35] J. Guo, L. Ma, and D. Zhang, "Management and utilization of high-pressure floor-confined water in deep coal mines," *Mine Water and the Environment*, vol. 38, no. 4, pp. 780–797, 2019.

[36] J. Sun, Y. Hu, and G. Zhao, "Relationship between water inrush from coal seam floors and main roof weighting," *International Journal of Mining Science and Technology*, vol. 27, no. 5, pp. 873–881, 2017.

[37] X. J. Qian and S. P. Minggao, *Mining Pressure and Strata Control*, China University of mining and Technology Press, Xuzhou, China, 2010.

[38] Z. Wen, S. Jing, Y. Jiang et al., "Study of the fracture law of overlying strata under water based on the flow- stress-damage model," *Geofluids*, vol. 2019, Article ID 3161852, 12 pages, 2019.

[39] K. Aoyagi and E. Ishii, "A method for estimating the highest potential hydraulic conductivity in the excavation damaged zone in mudstone," *Rock Mechanics and Rock Engineering*, vol. 52, no. 2, pp. 385–401, 2019.

[40] S. J. Li, X. T. Feng, C. Y. Wang, and J. A. Hudson, "ISRM suggested method for rock fractures observations using a borehole digital optical televiewer," *Rock Mechanics and Rock Engineering*, vol. 46, no. 3, pp. 635–644, 2013.

[41] Y. M. Zhao, X. T. Feng, Q. Jiang et al., "Large deformation control of deep roadways in fractured hard rock based on cracking-restraint method," *Rock Mechanics and Rock Engineering*, vol. 54, no. 5, pp. 2559–2580, 2021.